




Improper relaxor state in $(\text{Ca}_{1-x}\text{Sr}_x)_8[\text{AlO}_2]_{12}(\text{MoO}_4)_2$ Hiroki Nakamori, Ichiro Terasaki , and Hiroki Taniguchi ^{*}
Department of Physics, Nagoya University, Nagoya 464-8602, Japan (Received 10 July 2020; revised 30 August 2020; accepted 25 September 2020; published 22 October 2020)

Dielectric and elastic properties of aluminate-sodalite-type oxides, $(\text{Ca}_{1-x}\text{Sr}_x)_8[\text{AlO}_2]_{12}(\text{MoO}_4)_2$ with $x = 1/16$ and $1/4$, are investigated in the present study. A well-defined improper ferroelectric phase transition is demonstrated in the composition of $x = 1/16$ by the onset of spontaneous strain and sharp anomalies in the dielectric and elastic responses around 600 K. As the Sr concentration increases to $x = 1/4$, strong frequency dispersion appears in the dielectric and elastic responses, indicating that the system changes into a short-range ordered state. The dielectric and elastic anomalies are found to follow a single Vogel-Fulcher equation over a wide frequency range from 10^{-1} to 10^6 Hz. The present results suggest an improper relaxor state at the composition of $x = 1/4$, in which polar nanoregions form under spatially heterogeneous strain due to differences in the local coordination environments around Ca and Sr.

DOI: [10.1103/PhysRevMaterials.4.104413](https://doi.org/10.1103/PhysRevMaterials.4.104413)

I. INTRODUCTION

Nonperovskite-type oxides have recently attracted increasing attention as a new frontier of ferroelectric materials. A recent report of ferroelectricity in fluorite-type oxides, for instance, has inspired the development of novel nonvolatile memories [1–3]. Several oxides with a κ - Al_2O_3 -type structure show an unconventional polarization mechanism, providing a different design principle for ferroelectric materials [4–6]. Since the discovery of high- T_c ferroelectricity in Bi_2SiO_5 , in which the polar fluctuation of one-dimensional SiO_4 chains drives ferroelectric phase transition [7–10], materials with a network of oxygen tetrahedra have become fascinating targets when developing new ferroelectrics. A close competition between ferroelectric and antiferroelectric instabilities found in Bi_2SiO_5 suggests the rich tunability of dielectric properties in this system [11].

Aluminate-sodalite-type compounds are potential candidates in the design of nonperovskite-type ferroelectric materials with unique functionalities. Their general composition is given by $M_8[\text{AlO}_2]_{12}(\text{XO}_4)_2$, and there are plenty of available elements for M and X sites. Depending on the selection of M - and X -site elements, various crystal structures and physical properties emerge [12–17]. An improper ferroelectric phase transition was found in $\text{Sr}_8[\text{AlO}_2]_{12}(\text{CrO}_4)_2$ [18]. This improper ferroelectricity was also reported in $(\text{Ca}_{1-x}\text{Sr}_x)_8[\text{AlO}_2]_{12}(\text{WO}_4)_2$, $(\text{Ca}_{1-x}\text{Sr}_x)_8[\text{AlO}_2]_{12}(\text{MoO}_4)_2$, and $(\text{Ca}_{1-x}\text{Sr}_x)_8[\text{AlO}_2]_{12}(\text{SO}_4)_2$ at Ca-rich compositions [19–21]. To elucidate the mechanism of improper ferroelectricity, the correlation among multiple physical quantities is of primary interest in aluminate-sodalite-type oxides. It was suggested that, particularly in $(\text{Ca}_{1-x}\text{Sr}_x)_8[\text{AlO}_2]_{12}(\text{SO}_4)_2$, an antiferroelectric phase transition takes place at Sr-rich compositions [22]. From an application viewpoint, a

pyroelectric energy harvesting property with excellent efficiency has been proposed in $(\text{Ca}_{1-x}\text{Sr}_x)_8[\text{AlO}_2]_{12}(\text{WO}_4)_2$ and $(\text{Ca}_{1-x}\text{Sr}_x)_8[\text{AlO}_2]_{12}(\text{MoO}_4)_2$ [19,20]. Furthermore, direct observations of the P - E hysteresis loop have recently been achieved in multilayer ceramics capacitors of $(\text{Ca}_{1-x}\text{Sr}_x)_8[\text{AlO}_2]_{12}(\text{MoO}_4)_2$, paving the way for their practical applications [23].

In the present study, we investigated the dielectric and elastic properties of $(\text{Ca}_{1-x}\text{Sr}_x)_8[\text{AlO}_2]_{12}(\text{MoO}_4)_2$ with $x = 1/16$ and $1/4$ as a function of temperature to obtain insight into the phase transition properties of aluminate-sodalite-type oxides. $(\text{Ca}_{1-x}\text{Sr}_x)_8[\text{AlO}_2]_{12}(\text{MoO}_4)_2$ is hereafter abbreviated as (CS)AM- x . In contrast to the sharp anomalies in the dielectric and elastic responses observed in (CS)AM-1/16, broad and frequency-dependent dielectric/elastic anomalies have been found in (CS)AM-1/4, indicating that the system results in a short-range-ordered state in a low-temperature region. Since the Ca end-member of (CS)AM- x undergoes an improper ferroelectric phase transition [20], the short-range-ordered state in (CS)AM-1/4 is suggested to be a so-called improper relaxor, where polar nanoregions are collaterally induced by short-range-ordering of a certain primary-order parameter different from polarization.

II. EXPERIMENTAL METHODS

(CS)AM- x polycrystalline samples were synthesized with a conventional solid-state reaction method. Stoichiometric powder mixtures of CaCO_3 (99.99%), SrCO_3 (99.9%), Al_2O_3 (99.99%), and MoO_3 (99.9%) were ground with an agate mortar and a pestle in ethanol and pressed into the shape of a rod. The rods were fired at 1400 °C for 12 h, followed by furnace cooling to room temperature. The sintered rods were sliced using a diamond saw (Model 650, South Bay Technology) for the elastic and dielectric measurements. Pieces of the samples were reground and subjected to powder x-ray-diffraction

^{*}Corresponding author: hiroki_taniguchi@cc.nagoya-u.ac.jp

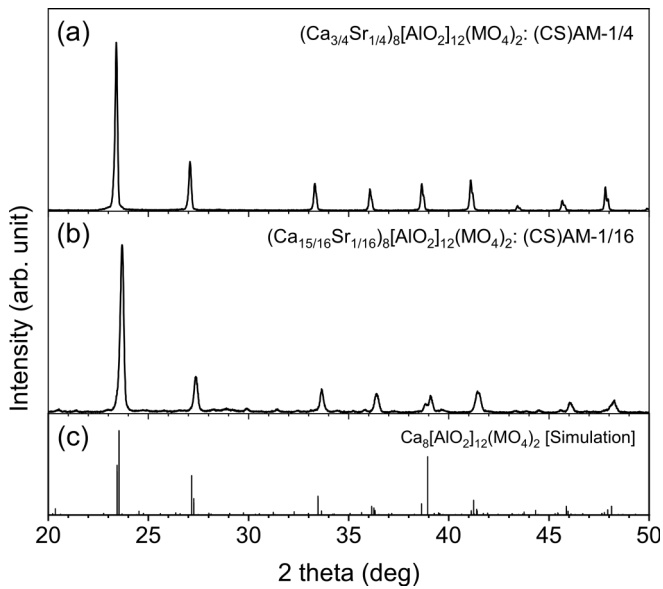


FIG. 1. Powder x-ray-diffraction patterns of (a) (CS)AM-1/4 and (b) (CS)AM-1/16, observed at room temperature. (c) The calculated pattern for the Ca end-member.

measurements using a Miniflex600 (RIGAKU) to check the quality of the samples.

Dielectric measurements were performed with a precision LCR meter 4284A (Hewlett Packard) on the samples with Ag electrodes baked to both surfaces. The temperature of the samples was controlled by THMS600 (LINKAM). Elastic properties were measured using DMA Q800 (TA Instruments) with a single cantilever mode. The dimensions of the samples used for the elastic measurements were $300 \times 7 \times 0.6 \text{ mm}^3$. Note that the temperature dependence of the dielectric and elastic properties was investigated on cooling.

III. RESULTS AND DISCUSSIONS

Figures 1(a) and 1(b) show powder x-ray-diffraction patterns of (CS)AM-1/4 and (CS)AM-1/16 observed over a 2θ range from 20° to 50° . The overall features of the diffraction profiles for both samples agree with the calculated pattern for the Ca end-member shown in Fig. 1(c), indicating that the present samples have sufficient quality for dielectric and elastic measurements. Under close examination of the diffraction profiles of (CS)AM-1/4 and (CS)AM-1/16, several peaks are seen to disappear in (CS)AM-1/4. Furthermore, split peaks, for instance around $2\theta \sim 39^\circ$, merge into single peaks as x increases from 1/16 to 1/4. These results suggest that a macroscopic symmetry at room temperature increases with the Sr substitution.

The dielectric responses of (CS)AM-1/16 and (CS)AM-1/4 are presented in Figs. 2(a)–2(d) as a function of temperature. Each dielectric permittivity is shown in Figs. 2(a) and 2(c), whereas the (dielectric) loss tangent, $\tan \delta$, is shown in Figs. 2(b) and 2(d). All measurements were performed at several frequencies, 10^3 , 10^4 , 10^5 , and 10^6 Hz, to investigate the frequency dispersion of the dielectric response. As shown in Fig. 1(a), a sharp peak is seen at 566 K on cooling. This peak indicates the ferroelectric phase transition of

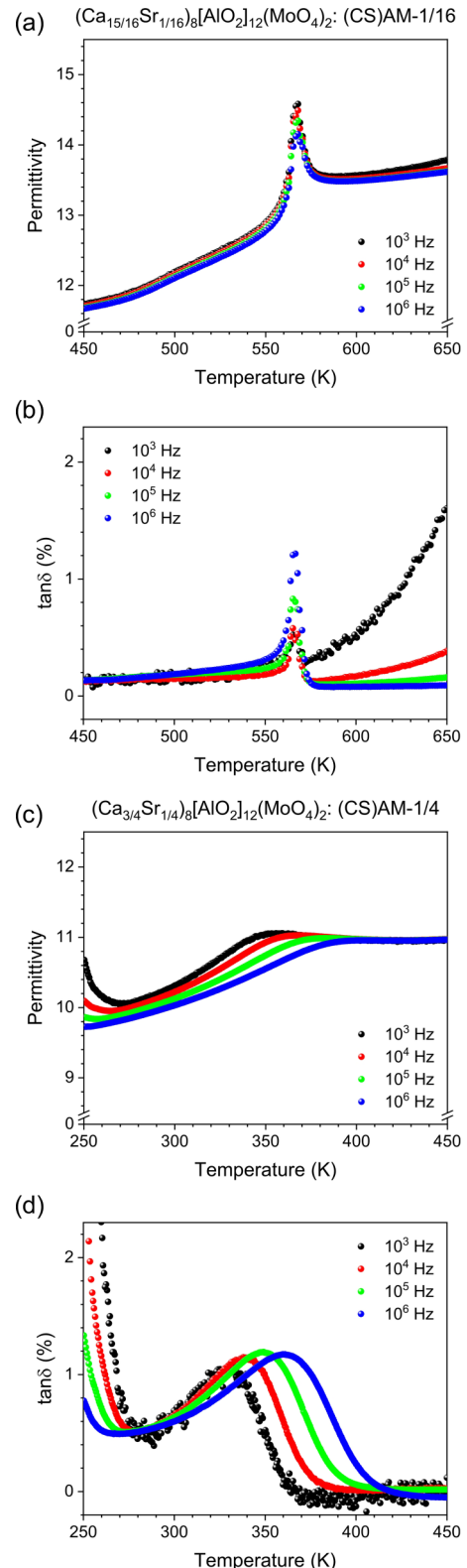


FIG. 2. Temperature dependence of dielectric responses observed at frequencies 10^3 , 10^4 , 10^5 , and 10^6 Hz in (CS)AM- x with (a),(b) $x = 1/16$ and (c),(d) $x = 1/4$. Panels (a),(c) and (b),(d) present the permittivity and $\tan \delta$, respectively.

(CS)AM-1/16. The permittivity culminates with a value of approximately 14.5, which is considerably smaller than the

typical value for a conventional proper ferroelectric phase transition. This result suggests the improper nature of the ferroelectric phase transition in (CS)AM-1/16, as also claimed in previous studies [19–22]. Synchronized with the permittivity anomaly, a distinct cusp also appears in the temperature dependence of $\tan \delta$, as presented in Fig. 2(b). Note that little frequency dispersion is seen in the dielectric anomalies observed in (CS)AM-1/16, indicating an onset of long-range ordering at the phase transition. In the (CS)AM-1/4, on the other hand, there is contrasting behavior in the temperature dependence of the dielectric response. As presented in Fig. 2(c), the peaklike anomaly of permittivity, which is seen around 350 K, strongly broadens. The corresponding anomaly in $\tan \delta$ shown in Fig. 2(d) also spreads over several tens of degrees Kelvin. The most significant variation due to the increment of x is the appearance of frequency dispersion in the dielectric anomaly. As presented in Figs. 2(c) and 2(d), the specific temperatures at which the permittivity and the $\tan \delta$ culminate increase as the measurement frequency increases. Such behavior is typically seen when the macroscopic phase transition is perturbed by some sort of disorder to render the system short-range ordered. The extra anomaly observed around 250 K is an extrinsic signal due to the slight humidity of the sample. Note here that the dielectric anomalies in CSAM-1/16 and CSAM-1/4 are discussed under the assumption that they stem from the same phase transition, although the transition temperatures for CSAM-1/16 and CSAM-1/4 are largely different. This can be justified by the results of dielectric measurements on CSAM- x ($x = 0.10, 0.15,$ and 0.20), where a systematic variation of the dielectric anomaly has been found with a progressive increase of Sr content x , as shown in Fig. 3.

Since (CS)AM- x undergoes an improper ferroelectric phase transition, of which the primary order parameter is other than polarization, the dielectric measurements give an indirect clue to the mechanism of phase transition. We thus performed elastic measurements to obtain complementary information to the dielectric response. Figures 4(a)–4(d) present the temperature dependence of the storage modulus [Figs. 4(a) and 4(c)] and (elastic) loss tangent, $\tan \delta$ [Figs. 4(b) and 4(d)], of (CS)AM-1/16 and (CS)AM-1/4 observed with load frequencies of 0.1, 0.3, 1.0, 3.0, and 10.0 Hz. The insets in Figs. 4(c) and 4(d) denote magnified views for the temperature range over which the elastic anomalies were found. As shown in Fig. 4(a), a pair of sharp dips were detected in the storage modulus at 566 and 561 K on cooling. These anomalies indicate that two phase transitions take place successively in a narrow temperature range. Note that the elastic anomaly observed at the lower temperature is not detected in the dielectric measurements. A reason for this discrepancy is probably due to the difference in their phase-transition properties. In the Ca end-member of (CS)AM- x , there are three phase transitions above room temperature with successive changes of symmetry: $I\bar{4}3m$ to $P\bar{4}c2(1)$ at $T_1 = 624$ K, $P\bar{4}c2(1)$ to $P\bar{4}c2(2)$ at $T_2 = 614$ K, and $P\bar{4}c2(2)$ to $Aea2$ at $T_3 = 590$ K [24]. Among these transitions, the structural variation across T_2 is the slightest from the viewpoint of crystal symmetry. Therefore, it would be reasonable to assign T_2 to the lower-temperature elastic anomaly at 561 K, which has a corresponding dielectric anomaly below the detection limit

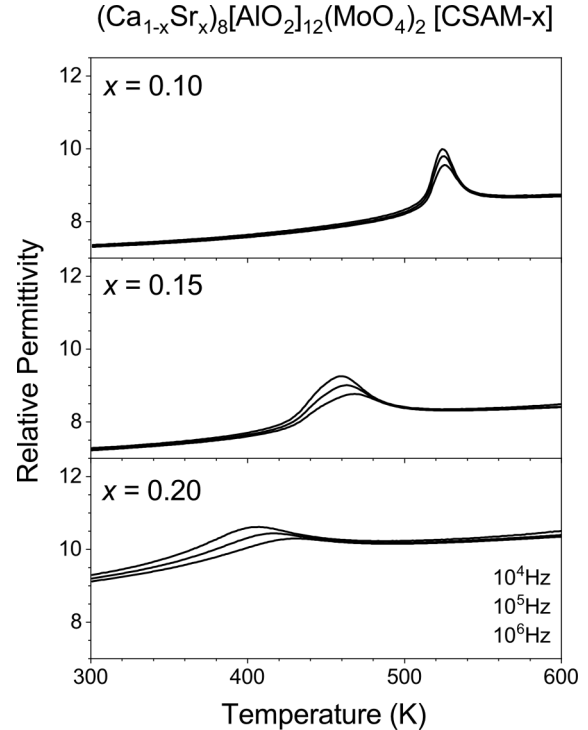


FIG. 3. Temperature dependence of dielectric permittivity for (CS)AM- x ($x = 0.10, 0.15,$ and 0.20), which was measured at the frequencies of $10^4, 10^5,$ and 10^6 Hz.

of the present dielectric measurement. Then, the higher one at 566 K can automatically be attributed to T_1 . Signs of T_1 and T_2 have also been found in the temperature dependence of elastic $\tan \delta$, as presented in Fig. 4(b). Note here that a weak and broad bump can be seen in the temperature dependence of the storage modulus around 500 K. This anomaly has been suggested to be a trace of T_3 . With increasing x to 1/4, as shown in Fig. 4(c), these anomalies merge into a single broad bump. The inset shows that the minimum of the broad bump shifts to a higher temperature as the load frequency increases. This feature is consistent with that observed in the dielectric measurements, indicating again the short-range-ordered state of the system. This strong frequency dispersion has also been seen in the anomaly of elastic $\tan \delta$, as shown in Fig. 4(d). It should be mentioned here that, as described above, the crystal symmetries for the two intermediate phases were proposed to be nonpolar $P\bar{4}c2$ [24]. If this is true, then the phase transition at T_1 is not the improper ferroelectric phase transition. However, the previous pyroelectric measurement for CSAM-0.16 has clearly demonstrated the polar symmetry below T_1 [20]. Although further investigations are necessary to determine the crystal structures below T_1 conclusively, the misassignment of crystal symmetries for the intermediate phases has little influence on the present discussion, since the structural variation across T_2 is subtle in any case.

Figure 5 shows the temperature dependence of the shear strain for (CS)AM-1/16 and (CS)AM-1/4, which were measured on heating without mechanical stress after cooling under the application of shear stress at 10 MPa. In (CS)AM-1/16, as shown in the figure, spontaneous strain disappears at $T_1 = 566$ K, synchronized with the anomalies in the dielectric per-

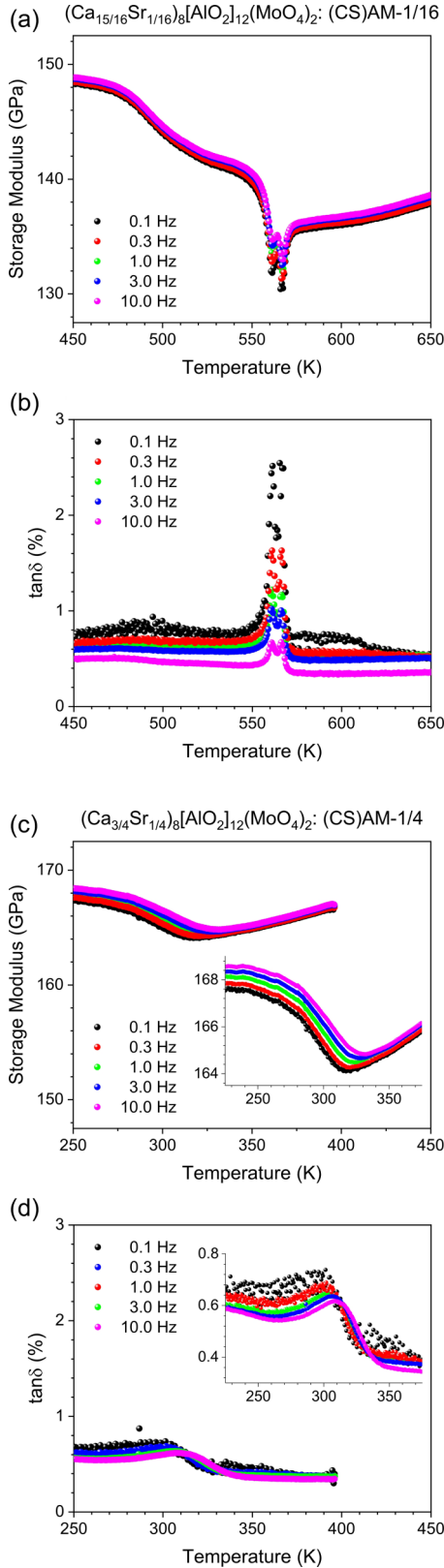


FIG. 4. Temperature dependence of the elastic responses observed with several frequencies in (CS)AM- x with (a),(b) $x = 1/16$ and (c),(d) $x = 1/4$. Panels (a),(c) and (b),(d) present the storage modulus and $\tan \delta$, respectively. Insets in panels (c) and (d) present magnified views.

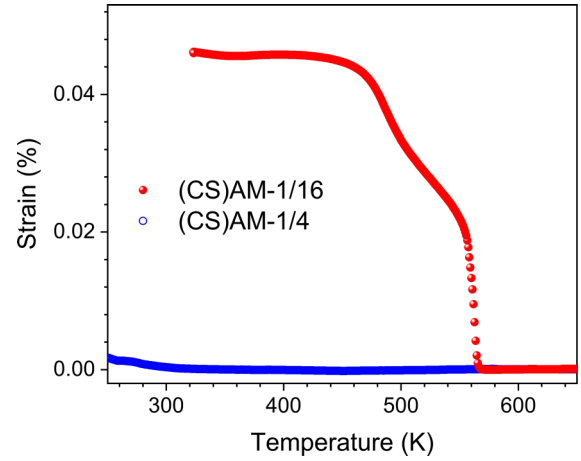


FIG. 5. Temperature dependence of the shear strain observed in (CS)AM-1/16 and (CS)AM-1/4, which was measured on heating without bias stress after cooling under the loading of bias stress.

mittivity and storage modulus. This result demonstrates that the phase transition at T_1 has a ferroelastic nature. Furthermore, an additional bump is seen around 500 K, suggesting successive evolution of the strain at T_3 . As for T_2 , on the other hand, little anomaly was found in the present study, probably due to overlap with the anomaly at T_1 and/or a change in the crystal structure at T_2 that is too subtle to be detected. In (CS)AM-1/4, on the other hand, only a slight strain was detected below the temperature around which the dielectric and elastic anomalies were found. Such a negligibly small spontaneous strain along with the dispersive anomaly in the susceptibility also manifests the short-range-ordered relaxor-like state of (CS)AM-1/4.

To obtain further insight into the phase transition of (CS)AM-1/4, the dielectric and elastic anomalies were analyzed quantitatively. Plotted in Fig. 6 are the test frequencies against the inverse of the specific temperatures for (CS)AM-1/4 at which extrema were observed in the temperature dependence of dielectric permittivity and storage modulus. As shown in the figure, the data points deviate from the Arrhenius-type behavior that is denoted by the broken line. This trend implies the existence of interacting clusters of nanoscopic scale in the system. To examine this possibility, further analyses were performed with the Vogel-Fulcher law,

$$\omega = \omega_0 \exp \left[\frac{-E_a}{k_B(T_0 - T_f)} \right],$$

where E_a , T_0 , T_f , and ω_0 are the activation energy necessary for reorientation of clusters, the temperature at which the extremum is observed, the freezing temperature of fluctuating clusters, and a high-frequency limit of cluster reorientation, respectively. As shown by the solid curve in Fig. 6, the data points were able to be reproduced by a single Vogel-Fulcher equation over the entire frequency range covered in the present experiments with the dielectric and elastic measurements. This result suggests dielectric and elastic interactions among the nanoclusters in (CS)AM-1/4. Note that, although the best fit was obtained with seemingly reasonable values for E_a and T_f of 545 meV and 179.5 K, respectively,

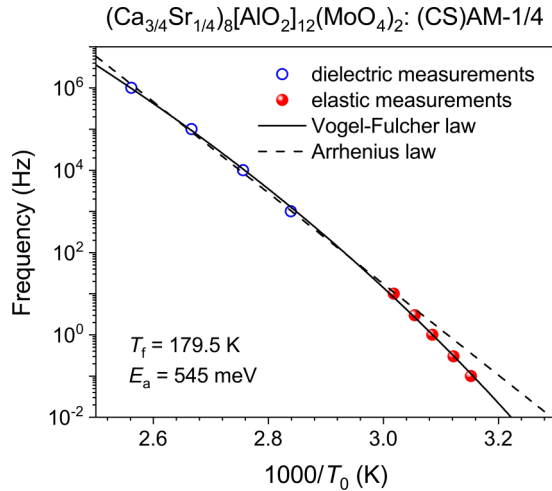


FIG. 6. The measurement frequencies used in the dielectric and elastic measurements vs the inverse of the specific temperatures obtained in (CS)AM-1/4 at which extrema were observed in the temperature dependence of dielectric permittivity and storage modulus. The solid curve denotes the most adequate fit obtained with the Vogel-Fulcher law (see text for detail).

ω_0 resulted in an unreasonably large value on the order of 10^{19} Hz. There would thus be an unconventional interaction among nanoclusters in (CS)AM-1/4 beyond the basis of the Vogel-Fulcher law. As the ferroelectricity in (CS)AM- x is improper, the interaction of clusters and their dynamics are expected to be different from those for the canonical relaxor, which has nanoclusters that interact through the strong polar fluctuation in the matrix of large permittivity [25–28]. Since the primary order parameter for the phase transitions of the aluminato-sodalite-type family was proposed to be the orientational ordering of the XO_4 anions [13,19], mutual correlation among MoO_4 anions would play a significant role in the system of (CS)AM- x .

To discuss the correlation in orientations of MoO_4 anions, here we focus on the coordination environments of Ca/Sr cations. Figure 7 depicts schematic illustrations for local structures around Ca and Sr in both end-members of (CS)AM- x , $\text{Ca}_8[\text{AlO}_2]_{12}(\text{MoO}_4)_2$, and $\text{Sr}_8[\text{AlO}_2]_{12}(\text{MoO}_4)_2$, according to their crystal structures reported in previous studies [13,24]. The left side of the figure presents the high-temperature $I\bar{4}3m$ and the low-temperature $Aea2$ phases for the Ca end-member, while the right side shows the high-temperature $Im\bar{3}m$ and the low-temperature $I4_1/acd$ phases for the Sr end-member. Illustrations in the upper and lower rows are respectively projected onto planes perpendicular and parallel to a [111] direction of the cubic $Im\bar{3}m$ structure, which has crystallographic axes indicated by arrows in the figure. In the cubic phases with $I\bar{4}3m$ and $Im\bar{3}m$ symmetries, as shown in the upper row of Fig. 7, Ca/Sr locates at the center of a noncentrosymmetric/symmetric hexagonal configuration of six oxygen anions, which are involved in a CaO_8 (SrO_8) polyhedron. As depicted in the lower row, the CaO_8 (SrO_8) polyhedron shares top and bottom apical oxygens with MoO_4 tetrahedra in (CS)AM- x . Due to this characteristic local structure, the difference in the site symmetry between Ca and Sr in the high-temperature phase exerts a

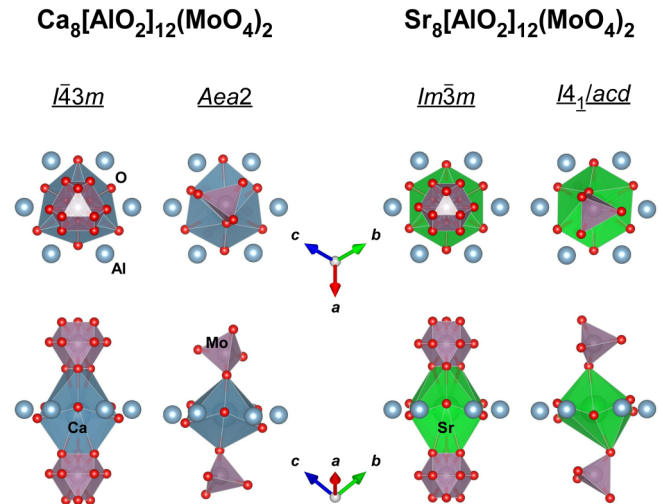


FIG. 7. Schematic illustrations of the local environments around Ca and Sr in the Ca and Sr end-members of (CS)AM- x showing their high- and low-temperature structures. See text for details.

significant influence on the ordering of MoO_4 tetrahedra in the low-temperature phase. In the cubic phases, the MoO_4 tetrahedra reorient among six equivalent orientations due to a strong thermal fluctuation [12]. When the thermal fluctuation is sufficiently suppressed, each MoO_4 tetrahedron freezes in the most comfortable orientation in association with the deformation of the corner-shared CaO_8 (SrO_8) polyhedron. In the end-member compositions, the freezing of reorientation results in a certain ordering pattern of MoO_4 tetrahedra with a long-range correlation, to induce the macroscopic structural phase transition into the lower symmetry phase. Examples of the resulting MoO_4 orientations in Ca and Sr end-members are depicted in Fig. 7 for the $I4_1/acd$ and $Aea2$ structures. In the mixed composition of Ca and Sr, on the other hand, the long-range periodic arrangement of MoO_4 orientations is expected to be strongly perturbed, since the most comfortable orientation of the MoO_4 tetrahedron crucially depends on the shape of the corner-shared polyhedra. Thus, the geometric difference between CaO_8 and SrO_8 would induce disordering in the MoO_4 orientations. Such a specific local situation of (CS)AM- x would cause short-range-ordered “orientational” nanoclusters with an unconventional interaction among them through the deformation of adjacent coordination polyhedra.

IV. CONCLUSIONS

Dielectric and elastic properties of the aluminato-sodalite-type oxides $(\text{Ca}_{1-x}\text{Sr}_x)_8[\text{AlO}_2]_{12}(\text{MoO}_4)_2$ ((CS)AM- x) with $x = 1/16$ and $1/4$ have been investigated as a function of temperature over the wide frequency range from 10^{-1} to 10^6 Hz. In contrast to the well-defined improper ferroelectric phase transitions in (CS)AM-1/16, the diffusive phase transition with short-range ordering was demonstrated in (CS)AM-1/4 by the broad and frequency-dependent anomalies found in dielectric and elastic responses. The observed frequency dispersion of dielectric/elastic anomalies imply an unconventional interaction among nanoclusters in the short-

range-ordered state found in (CS)AM-1/4. The origin of nanoclusters is suggested to be correlated orientations of MoO_4 tetrahedra, which are perturbed by geometric heterogeneity due to the difference between shapes of the corner-shared CaO_8 and SrO_8 polyhedra. As the freezing of the MoO_4 orientation is the primary trigger for the improper ferroelectric phase transition of (CS)AM- x , the ground state of (CS)AM-1/4 is the so-called improper relaxor state, which is induced by the freezing of the MoO_4 fluctuation with the short-range-ordered arrangement of their orientations. The peculiar local environment of the aluminate-sodalite-type oxides

enables intuitive control of the spatial correlation of polarization with the geometric design of the constituent polyhedra. This provides a useful platform for the development of ferroelectric materials.

ACKNOWLEDGMENT

This work was partially supported by the MEXT Elements Strategy Initiative to Form Core Research Center, Grant No. JPMXP0112101001.

- [1] T. S. Börscke, J. Müller, D. Bräuhäus, U. Schröder, and U. Böttger, Ferroelectricity in hafnium oxide thin films, *Appl. Phys. Lett.* **99**, 102903 (2011).
- [2] J. Müller, T. S. Börscke, U. Schröder, S. Mueller, D. Bräuhäus, U. Böttger, L. Frey, and T. Mikolajick, Ferroelectricity in Simple Binary ZrO_2 and HfO_2 , *Nano Lett.* **12**, 4318 (2012).
- [3] P. Polakowski and J. Müller, Ferroelectricity in undoped hafnium oxide, *Appl. Phys. Lett.* **106**, 232905 (2015).
- [4] Y. Hamasaki, T. Shimizu, S. Yasui, T. Taniyama, and M. Itoh, Evidence of ferroelectricity in ferrimagnetic κ - Al_2O_3 -type $\text{In}_{0.25}\text{Fe}_{1.75}\text{O}_3$ films, *Appl. Phys. Lett.* **109**, 162901 (2016).
- [5] T. Katayama, S. Yasui, Y. Hamasaki, T. Shiraiishi, A. Akama, T. Kiguchi, and M. Itoh, Ferroelectric and Magnetic Properties in Room-Temperature Multiferroic $\text{Ga}_x\text{Fe}_{2-x}\text{O}_3$ Epitaxial Thin Films, *Adv. Funct. Mater.* **28**, 1704789 (2018).
- [6] T. Katayama, S. Yasui, T. Osakabe, Y. Hamasaki, and M. Itoh, Ferrimagnetism and ferroelectricity in Cr-substituted GaFeO_3 epitaxial films, *Chem. Mater.* **30**, 1436 (2018).
- [7] H. Taniguchi, A. Kuwabara, J. Kim, Y. Kim, H. Moriwake, S. Kim, T. Hoshiyama, T. Koyama, S. Mori, M. Takata, H. Hosono, Y. Inaguma, and M. Itoh, Ferroelectricity driven by twisting of silicate tetrahedral chains, *Angew. Chem. Int. Ed.* **52**, 8088 (2013).
- [8] Y. Kim, J. Kim, A. Fujiwara, H. Taniguchi, S. Kim, H. Tanaka, K. Sugimoto, K. Kato, M. Itoh, H. Hosono, and M. Takata, Hierarchical dielectric orders in layered ferroelectrics Bi_2SiO_5 , *IUCr* **1**, 160 (2014).
- [9] D. Seol, H. Taniguchi, J. Hwang, M. Itoh, H. Shin, S. Kim, and Y. Kim, Strong anisotropy of ferroelectricity in lead-free bismuth silicate, *Nanoscale* **7**, 11561 (2015).
- [10] J. Park, B. G. Kim, S. Mori, and T. Oguchi, Tetrahedral tilting and ferroelectricity in Bi_2AO_5 ($A = \text{Si}, \text{Ge}$) from first principles calculations, *J. Solid State Chem.* **235**, 68 (2016).
- [11] A. Girard, H. Taniguchi, S. M. Souliou, M. Stekiel, W. Morgenroth, A. Minelli, A. Kuwabara, A. Bosak, and B. Winkler, Competing structural instabilities in Bi_2SiO_5 , *Phys. Rev. B* **98**, 134102 (2018).
- [12] W. Depmeier, Aluminate sodalites - a family with strained structures and ferroic phase transitions, *Phys. Chem. Miner.* **15**, 419 (1988).
- [13] W. Depmeier and W. Bührer, Aluminate sodalites: $\text{Sr}_8[\text{Al}_{12}\text{O}_{24}](\text{MoO}_4)_2$ (SAM) at 293, 423, 523, 623 and 723 K and $\text{Sr}_8[\text{Al}_{12}\text{O}_{24}](\text{WO}_4)_2$ (SAW) at 293 K, *Acta Cryst.* **B47**, 197 (1991).
- [14] X. Hu, W. Depmeier, G. Wildermuth, and S. Doyle, New phase transitions in the solid solution system $(\text{Ca}_{1-x}\text{Sr}_x)_8[\text{Al}_{12}\text{O}_{24}](\text{WO}_4)_2$, *Z. Kristallogr.* **211**, 679 (1996).
- [15] D. M. Többsen and W. Depmeier, Intermediate phases in the Ca-rich part of the system $(\text{Ca}_{1-x}\text{Sr}_x)_8[\text{Al}_{12}\text{O}_{24}](\text{WO}_4)_2$, *Z. Kristallogr.* **213**, 522 (1998).
- [16] R. X. Fischer and W. H. Baur, Symmetry relationships of sodalite (SOD) - type crystal structures, *Z. Kristallogr.* **224**, 185 (2009).
- [17] S. Takeda, M. Colas, T. Asaka, P. Thomas, and K. Fukuda, Phase transformation of $\text{Ca}_4[\text{Al}_6\text{O}_{12}]\text{SO}_4$ and its disordered crystal structure at 1073 K, D. Kurokawa, *J. Solid State Chem.* **215**, 265 (2014).
- [18] J.-F. Rossignol, J.-P. Rivera, P. Tissot, and H. Schmid, Optical, dielectric and DSC studies of "yellow-type" aluminate sodalite $\text{Sr}_8[\text{Al}_{12}\text{O}_{24}](\text{CrO}_4)_2$, *Ferroelectrics* **79**, 197 (1988).
- [19] Y. Maeda, T. Wakamatsu, A. Konishi, H. Moriwake, C. Moriyoshi, Y. Kuroiwa, K. Tanabe, I. Terasaki, and H. Taniguchi, Improper Ferroelectricity in Stuffed Aluminate Sodalites for Pyroelectric Energy Harvesting, *Phys. Rev. Appl.* **7**, 034012 (2017).
- [20] T. Wakamatsu, K. Tanabe, I. Terasaki, and H. Taniguchi, Improper ferroelectrics as high-efficiency energy conversion materials, *Phys. Status Solidi RRL* **11**, 1770324 (2017).
- [21] T. Wakamatsu, G. Kawamura, T. Abe, S. Kawaguchi, C. Moriyoshi, Y. Kuroiwa, M. Itoh, I. Terasaki, and H. Taniguchi, Structural Phase transitions and possibility of the relaxor-like state in improper ferroelectric strontium-substituted calcium sulfoaluminates, *J. Phys. Soc. Jpn.* **88**, 034718 (2019).
- [22] T. Wakamatsu, G. Kawamura, T. Abe, Y. Nakahira, S. Kawaguchi, C. Moriyoshi, Y. Kuroiwa, I. Terasaki, and H. Taniguchi, Antiferroelectric to antiferroelectric-relaxor phase transition in calcium strontium sulfoaluminate, *Inorg. Chem.* **58**, 15410 (2019).
- [23] S. Hirose, T. Usui, M. Tanaka, Y. Katsuya, and H. Taniguchi, Ferroelectric and dielectric properties of improper ferroelectric $\text{CaSr}[\text{Al}_{12}\text{O}_{24}](\text{MoO}_4)_2$ multilayer capacitors, *J. Appl. Phys.* **128**, 094101 (2020).
- [24] S. van Smaalen, R. Dinnebier, H. Katzke, and W. Depmeiers, Structural characterization of the high-temperature phase transitions in $\text{Ca}[\text{Al}_{12}\text{O}_{24}](\text{MoO}_4)_2$ aluminate sodalite using X-ray powder diffraction, *J. Solid State Chem.* **129**, 130 (1997).
- [25] L. E. Cross, Relaxor ferroelectrics, *Ferroelectrics* **76**, 241 (1987).
- [26] A. A. Bokov and Z.-G. Ye, Recent progress in relaxor ferroelectrics with perovskite structure, *J. Mater. Sci.* **41**, 31 (2006).

- [27] V. Westphal, W. Kleemann, and M. D. Glinchuk, Diffuse Phase Transitions and Random-Field-Induced Domain States of the “relaxor” Ferroelectric $\text{PbMg}_{1/3}\text{Nb}_{2/3}\text{O}_3$, *Phys. Rev. Lett.* **68**, 847 (1992).
- [28] D. Fu, H. Taniguchi, M. Itoh, S. Koshihara, N. Yamamoto, and S. Mori, Relaxor $\text{Pb}(\text{Mg}_{1/3}\text{Nb}_{2/3})\text{O}_3$: A Ferroelectric with Multiple Inhomogeneities, *Phys. Rev. Lett.* **103**, 207601 (2009).